Korean J. Chem. Eng., 39(7), 1805-1820 (2022)
DOI: 10.1007/s11814-022-1101-8

pISSN: 0256-1115
eISSN: 1975-7220

Eco-friendly adsorption of dye pollutants by palygorskite in aqueous effluents: Experimental and computational studies

Anne Beatriz Figueira Câmara*,†, Rafael Viana Sales*, Carlos Vital dos Santos Júnior**, Miguel Angelo Fonseca de Souza****, Clenildo de Longe*, Thiago Medeiros Chianca*, Rosangela Dala Possa**, Luiz Carlos Bertolino***, and Luciene Santos de Carvalho*,†**

*Institute of Chemistry, Federal University of Rio Grande do Norte, Energetic Technologies Research Group, 59078-900, Natal, Brazil
**Mineral Technology Center, 21941-908, University City, Rio de Janeiro, Brazil
***Xingu Study Institute, Federal University of the South and Southeast of Pará, 68380-000, São Félix do Xingu-PA, Brazil
****Laboratory of Computational Chemistry, Institute of Chemistry, Federal University of Rio Grande do Norte, 59078-900, Natal, Brazil

(*Received 9 September 2021 • Revised 21 February 2022 • Accepted 4 March 2022*)

Abstract−Palygorskite clay mineral (Pal) was employed in the removal of Congo red (CR) and methylene blue (MB) dyes pollutants in aqueous effluents by the adsorption process. The materials, Pal raw and acid Pal (Apal), were characterized by SEM, EDX, XRD, XFR, FTIR, XPS and Raman spectroscopy techniques that evidenced the main active sites of clay mineral. Characterization data indicated that acid treatment caused a leaching process of metallic cations on the Pal surface. As result, the maximum adsorption capacity was increased from 11.3 to 120.5 $mg \cdot g^{-1}$ and from 2.7 to 238.1 $mg \cdot g^{-1}$ for MB and CR dyes, respectively. The regeneration result after five cycles was of 75% recovered to MB adsorption into Apal. Semi-empirical quantum mechanical (SQM) calculations were performed to identify the mechanism of interaction between the Pal surface and dyes. High correlation (R^2>0.99) was observed for the experimental data using the pseudo-second-order kinetic model, that were confirmed by computed enthalpy values (−298.7 to −84.5 $kJ \cdot mol^{-1}$), suggesting a chemisorption process as the determining step. Furthermore, the experimental and computational results indicated that the Pal also could work removing efficiently two dyes simultaneously with an adsorption capacity of 37.2 and 40.4 $mg \cdot g^{-1}$ for MB and CR, respectively.

Keywords: Palygorskite, Removal Dyes Pollutants, SQM Calculations, PM7 Method, Adsorption Equilibrium, Adsorption Kinetics

INTRODUCTION

The pollution of water sources caused by dye effluents is currently one of the biggest environmental and health problems. Dyes are highly soluble in water, have complex aromatic structures and xenobiotic properties which make them difficult to be degraded, thereby causing bioaccumulation in flora and fauna, in addition to being carcinogenic [1]. The main factor responsible for this contamination is industries which use the dyeing and/or finishing processes, such as textiles, paper and cellulose, paints and coatings, leather, and packaging, among others, by which about 70,000 tons/year of dye effluent is released from these industries and contaminates surface and groundwater [2]. These residues are dealt with in treatment centers or released directly into the environment, usually in water sources such as rivers, lakes and seas, causing harmful effects on living organisms [3].

Dyes and pigments can be divided into three categories according to their chemical structure and water solubility. These categories include cationic, anionic and non-ionic dyes, with the first being the most toxic [4]. Methylene blue (MB) is a cationic and non-biodegradable dye. The existence of 14 electrons delocalized in its structure makes this molecule readily aggregated and highly soluble in aqueous solutions [5]. Congo red (CR) is a classic anionic diazo dye, mainly used in dyeing paper and fabrics, including cotton, hemp and silk [6]. Azo dyes are known for their health risks due to their toxicity, mutagenicity and carcinogenicity [7].

Numerous technologies and methods are used to remove these compounds, such as biological, physical-chemical, chemical decomposition, oxidation process, enzymatic decomposition, electrochemical process, and adsorption with diverse materials as carbon-based nanomaterials, such as functionalized carbon nanotubes, magnetic polymer composite and clay mineral [3,8,9]. The adsorption process is the most used method to remove dyes from aqueous effluents, as it presents high efficiency, low cost and generates non-toxic waste [5]. Activated carbon from various biomasses, ion exchange resins, zeolites and clays stands out as the most used substance for this process. Clays and clay minerals are low-cost materials which are abundant in nature and present a high adsorption capacity. Smec-

Electronic supplementary material The online version of this article (https://doi.org/10.1007/s11814-022-1101-8) contains supplementary material, which is available to authorized users.

†To whom correspondence should be addressed.
E-mail: anne.beatrizfc@gmail.com, luciene_car@hotmail.com

tite [10], bentonite [11], and palygorskite [3] have been studied.

These clays have an affinity for dye adsorption in their natural forms due to their morphology, high surface area and ion exchange process. However, it is possible to enhance their adsorption capacity through chemical, physical or physical-chemical treatments or modifications, increasing the adsorption sites and providing the desired properties [11].

Palygorskite (Pal) is a low-cost hydrated magnesium aluminum silicate, with a needle-like structure which presents specific properties such as high surface area, moderated layer charge, high ion-exchange capability and active groups in its surface, conferring adsorption and catalytical properties to this clay mineral [12]. Indeed, the absorptive capacity of the Pal is being widely used to remove polluting dyes [13,14] and toxic metals such as Copper II [15], Arsenic [16], Iron III [17], and others. In addition, Pal has also been applied in the deproteinization of polysaccharides [18].

This paper contributes with the use of computational tools and equilibrium and kinetics mathematical models to investigate the removal of ionic dyes in aqueous effluents through adsorption process over a low-cost and environmentally friendly clay mineral adsorbent, palygorskite. Thus, the experimental data were applied to evaluate the adsorption mechanism and the diffusion of this adsorbate onto a Pal surface. PM7 semi-empirical computational methods were used to evaluate the interaction between the clay mineral and the dyes. The materials were characterized by Fourier transform infrared spectroscopy (FTIR), Raman spectroscopy, scanning electron microscopy (SEM), N_2 adsorption-desorption, X-ray photoelectron spectroscopy (XPS) and X-ray diffraction (XRD).

MATERIALS AND METHODS

1. Pre-treatment of Palygorskite

The samples of palygorskite clay mineral were obtained from deposits located in Guadalupe in the state of Piauí/Brazil and provided by the Mineral Technology Center (CETEM/RJ). 3 kg of this material was submitted to a process step aiming to eliminate impurities and concentrate the clay mineral. Pal was submitted to the wet granulometric classification using 45 μm and 20 μm sieves from Granutest (São Paulo, Brazil), in ambient conditions for the removal of magnetic minerals, as iron and titanium, present in the sample. Then, a fraction with less than 20 μm was submitted to magnetic separation in BOXMAG RAPID (Cardiff, UK) equipment with a high intensity field of approximately 15 kGauss. The non-magnetic and the magnetic fraction were filtered at 6 bar and dried in an oven at 60 °C. Fractions with less than 20 μm were disaggregated in a Retsch RS 200 brand mill (São Paulo, Brazil) for 2 minutes and 800 rpm.

Acid treated Pal was obtained to purify the clay mineral surface and about 5 g of this material was suspended in 100 mL of a 5 mol·L^{-1} hydrochloric acid (HCl, 37%, Vetec) solution and mixed under vigorous stirring at 40 °C for 4 h using an SL-91 stirring from Solab (São Paulo, Brazil) to obtain the acid-activated palygorskite. Then, the mixture was separated via centrifugation at 4,000 rpm for 5 min using a laboratory centrifuge from Daiki (São Paulo, Brazil), and the solids were washed with distilled water until the pH was equal to 7. The sample was subsequently dried in an oven at 80 °C for 12 h. This sample was denominated APal.

2. Dye Characterization

Methylene blue (MB) and Congo red (CR) ionic dyes were used to contaminate the effluent. The structure and relative parameters of these compounds are shown in Table 1.

The points were prepared from a sample of a 500 mg·g^{-1} solution for each dye (7.8×10^{-4} and 3.5×10^{-4} mol for MB and CR, respectively) and diluted until a minimum concentration of 25 mg·g^{-1}, totalizing seven points. The dyes in the samples were quantified using the ultraviolet and visible (UV-Vis) spectrophotometric technique with a Shimadzu UV-Vis 1800 spectrophotometer (Barueri, SP, Brazil). The calibration curves were prepared with wavelengths equal to 497 nm and 670 nm for the Congo red (CR) and methylene blue (MB) dyes, respectively.

3. Adsorbent Characterization

The XRD patterns of Pal and APal were obtained with a Bruker D2 Phaser equipment (Bruker AXS, Madison, WI, USA) coupled with a Lynxeye detector. The test was performed with copper radiation (CuKα, λ=1.54 Å) using a 2θ range of 5° and 5-90°, step of 0.01°, using a Ni filter, a current of 10 mA and voltage of 30 kV. Elemental analysis was conducted on a Bruker S2 Ranger X-ray fluorescence (XRF) spectrometer (Bruker AXS, Madison, WI, USA) using Pd or Ag radiation (max. power 50 W, max. voltage 50 kV, max. current 2 mA, XFlash® Silicon Drift Detector).

The N_2 adsorption/desorption method was used at 77 K to determine the textural properties of the adsorbents using QuantaChrome Nova 2200E equipment (Boynton Beach, FL, USA) following degassing of the samples at 300 °C for 4 h. The results of specific surface area (S_{BET}) were covered by the Brunauer - Emmett - Teller (BET) equation, while the pore size and volume were obtained by using

Table 1. Structural and molecular weight properties of the ionic dyes

Dye	Molecular structure	3D molecular structure	Molecular weight
Methylene blue (MB)	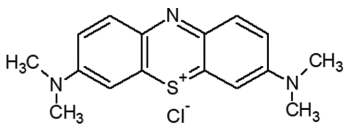	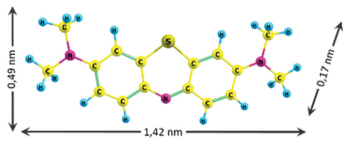	319.85
Congo red (CR)	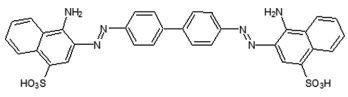	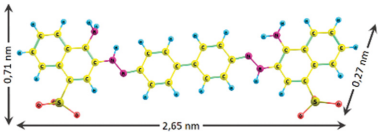	696.66

the Barrett Joyner - Halenda (BJH) method with a relative pressure (P/P_0) at 0.996.

FTIR analysis was conducted using Shimadzu IRAffinity-1 equipment (Columbia, MD, USA) with attenuated total reflectance (ATR). The spectra were obtained in the range of 700-4,000 cm^{-1} (4 cm^{-1} resolution and 32 scans). Raman spectra of the adsorbents were obtained using a confocal Raman microscope LabRAM HR Evolution from HORIBA Scientific (Palaiseau, France) by employing 758 nm line of an Argon laser. Scanning electron micrographs (SEM) with field emission gun (FEG) images were obtained using a ZEISS SEM-FEG AURIGA microscope (Carl Zeiss, Oberkochen, BW, Germany) linked to a Bruker Xflash Detector 410-M energy-dispersive X-ray (EDX) (Bruker AXS, Madison, WI, USA).

The X-ray photoelectron spectroscopy (XPS) results were obtained using a Physical Electronics PHI5700 spectrometer (Chanhassen, MN, USA) with non-monochromatic Mg-Kα radiation (300 W, 15 kV, 1,253.6 eV), constant energy of 29.35 eV and 720 μm diameter analysis area.

4. Data Treatment

4-1. Rietveld Refinement

Rietveld refinement was performed using the MAUD software to quantify the crystalline phases and the mineral composition present in the sample by the adjustment with references crystallographic charts [19]. The peak profiles were modelled using background and scale parameters and crystal structure analysis.

4-2. Deconvolution Test

Deconvolution was applied to evaluate the peaks present in the XRD pattern using PeakFit 4.12 software (Systat Software, Inc.) assuming Gaussian functions. The baseline was corrected by the second derivative with exponential method.

5. Kinetic Studies

The adsorption index of the dyes was investigated at different time intervals. Next, 25 mL of the solution containing 500 ppm of dyes and 0.3 g of the adsorbents were placed in glass vials. In addition, a dye mixture was made to study the synergisms between the two adsorbates using a solution of 250 ppm MB and 250 ppm, totalling a concentration of 500 ppm of the mixture of CR and 0.3 g of the adsorbents. Eight points were collected in each study and inserted into flasks. The study was carried out under rotation of 150 rpm and at room temperature (298 K) using an SL180/DT isothermal bath shaker (Solab) in different periods of time. The concentration of dyes remaining in the solutions was calculated using UV-Vis spectrophotometry, and the adsorption capacity of the adsorbents was calculated by three kinetic models.

The equations for pseudo-first-order, pseudo-second-order and Elovich kinetic models can be expressed according to Eqs. (1), (2) and (3), respectively [20]:

$$\log(q_e - q_t) = \log q_e - \frac{k_1 t}{2.303} \tag{1}$$

$$\frac{t}{q_t} = \frac{1}{k_2 q_e^2} + \frac{t}{q_e} \tag{2}$$

$$q_t = \frac{\ln(\alpha\beta)}{\beta} + \frac{1}{\beta}\ln t \tag{3}$$

In which: q_e and q_t are the amounts of sulfur compounds adsorbed (mg g^{-1}) on the adsorbent at equilibrium and at time t, respectively, k_1 (L min^{-1}) and k_2 (g mg^{-1} min^{-1}) are the rate constant of adsorption for pseudo-first order and pseudo-second order, respectively. α is the initial adsorption rate (mg g^{-1} min^{-1}), and β is related to the extent of surface coverage and activated energy for chemical adsorption (g·mg^{-1}).

Two models were investigated to evaluate the diffusion mechanism in the adsorption process. The intraparticle diffusion model usually involves four steps, which are the adsorbate transport from the bulk solution, film diffusion, intraparticle diffusion in the pores and in the solid phase, and the adsorption on the sites. This model can be calculated using the following equation [21]:

$$q_t = k_{id} t^{1/2} + C \tag{4}$$

In which: k_p is the intraparticle rate constant (g mg^{-1} $min^{-1/2}$) and C (mg g^{-1}) is the thickness of the boundary layer. The Boyd film-diffusion model assumes that the adsorbate diffusion through the boundary layer is the rate-limiting resistance to the adsorbent process [22]. This model is calculated by the following mathematic equation:

$$F = 1 - \frac{6}{\pi^2}\Sigma_{n=1}^{\infty}\frac{1}{n^2}\exp(-n^2 B_t) \tag{5}$$

In which: F (q_t/q_e) is a fractional uptake at a given time and B_t is a mathematical function of F according to:

$$\text{For } F>0.85,\ B_t = f(F) = -0.4977 - \ln(1-F) \tag{6}$$

$$\text{For } F<0.85,\ Bt = f(F) = \left(\sqrt{\pi} - \sqrt{\pi - \left(\frac{\pi^2 F}{3}\right)}\right)^2 \tag{7}$$

6. Equilibrium Adsorption Studies

The adsorption isotherms were acquired in a finite bathing system employing equivalent points for concentrations between 25 and 500 ppm in the dyes. Flasks with 250 mL were used with 25 mL of the dye solution and 0.3 g of the adsorbent. The system was left under stirring at 100 rpm on a shaker apparatus for three hours. The solutions were then centrifuged for 15 minutes at 1,000 rpm. The concentration of residual dyes in the solutions was verified with UV-Vis spectrophotometry, and the adsorbent adsorption capacity was calculated using three isotherm models. The linear mathematical equations for Langmuir, Freundlich and Temkin models are, respectively [23]:

$$\frac{C_e}{q_e} = \frac{1}{q_{max} K_L} + \frac{C_e}{q_{max}} \tag{8}$$

$$\log q_e = \log k_f + \frac{1}{n}\log C_e \tag{9}$$

$$q_e = B\ln K_t + B\ln C_e \tag{10}$$

In which: q_e is the amount of dyes adsorbed (mg g^{-1}); C_e is the equilibrium concentration (mg L^{-1}); K_L is the Langmuir equation constant (L mg^{-1}); q_{max} is the maximum adsorption capacity; k_f and n are Freundlich constants which represent adsorption capacity and adsorption intensity, respectively; K_t is the equilibrium binding constant (L mg^{-1}) in the Temkin equation; and B (B=RT/b), is related to the adsorption heat.

7. Desorption and Regeneration Studies

The dye-loaded Pal and APal adsorbents were used for desorption and reuse studies in consecutive five cycles for evaluating the regeneration ability of the adsorbents. Prior to that, the clay minerals were washed with distilled water to remove any non-adsorbed traces of the dyes (MB or CR) and were dried at 80 °C for 8 h. Thus, 0.3 g of the adsorbents was loaded with 25 mL from the dye solution (500 ppm) for 3 h. Then, was filtrated by centrifugation and mixed with HCl solution (0.1 mol·L^{-1}) for 4 h at 60 °C under stirring.

8. Computational Details

Fig. 1 displays the dimension of the selected palygorskite surface for the calculations. The crystallographic structure used for the palygorskite surface was obtained in the American Mineralogist Crystal Structure Database [24]. An idealized structural (with unit formula $(Mg_2,Al)Si_4O_{22}(OH)(HO_2)_4$) was used to represent the palygorskite surface. Discontinuous Mg/Al octahedral layers are sandwiched between continuous tetrahedral silicate (SiO_4) sheets in the palygorskite structure (see Fig. 1). Thus, zeolitic-like channels are

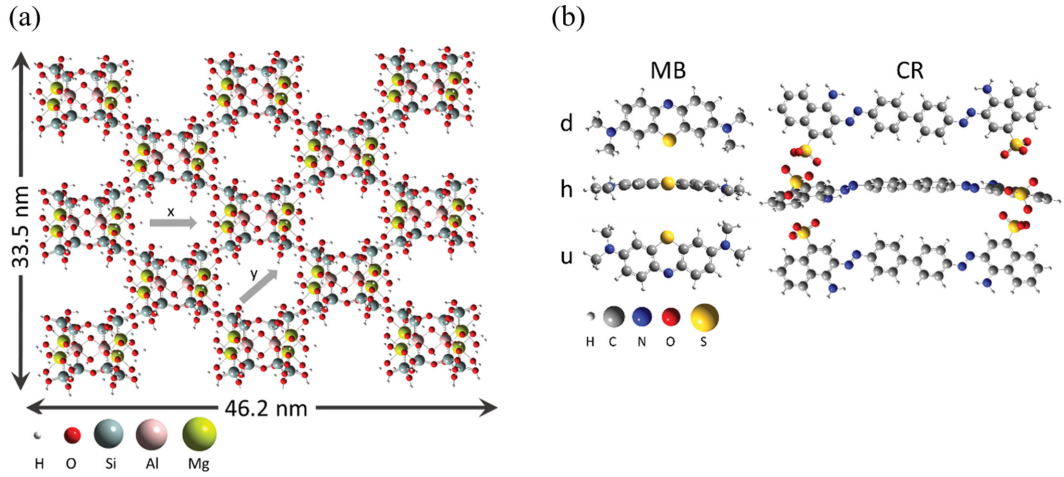

Fig. 1. (a) A 3a x 3b x 1c supercell of 1252 atoms was selected for the palygorskite surface, where a, b, and c are the lattice vectors. VESTA software was used to visualize and construct the structural model. (b) The CR and MB dye in the up (u) and down (d) vertical and horizontal (h) orientations along the x and y directions on the palygorskite surface.

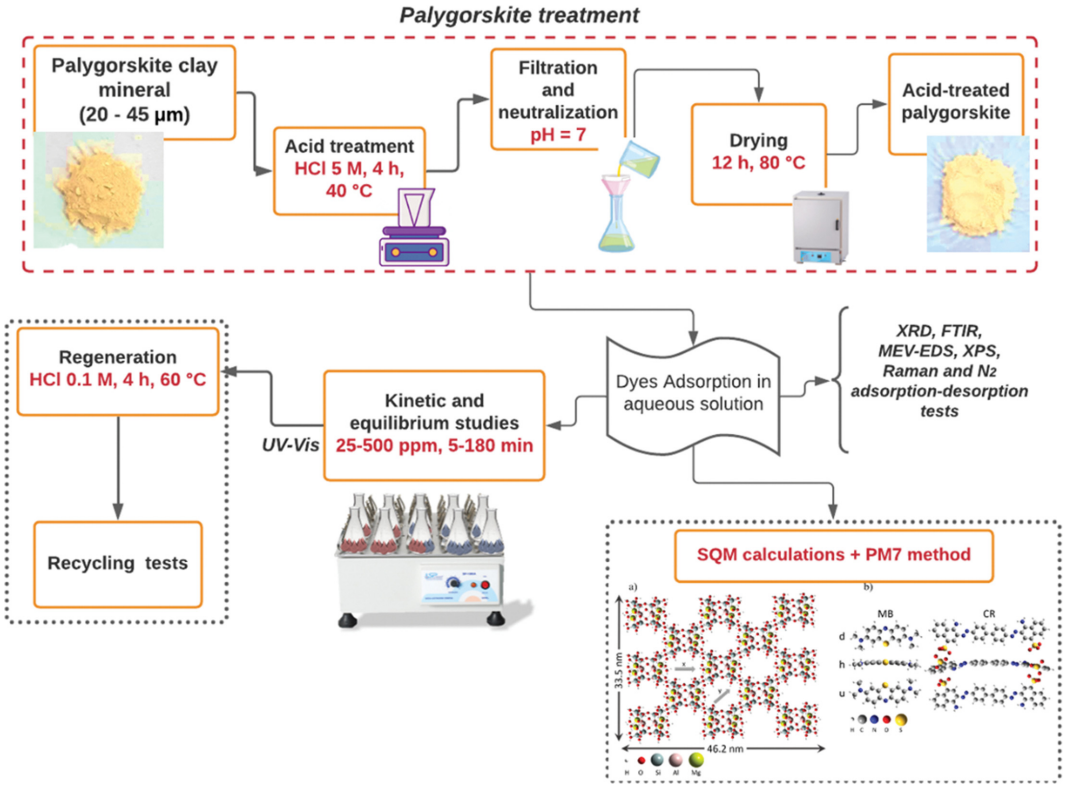

Fig. 2. Simplified flow diagram of the overall methodology.

generated along the c crystallographic direction as a result of the discontinuous Mg/Al octahedral layers. Zeolitic water molecules were eliminated in our model, which was consistent with the heat treatment carried out in this work. In addition, the dangling bonds at the edge and surface oxygen atoms were saturated with hydrogen. All hydrogen atoms included were fully relaxed with the GFN-force-field [25] using the xtb program package (Grimme-lab).

Semi-empirical quantum chemistry calculations were used to describe the adsorbate/adsorbent interactions between the palygorskite clay mineral and the dyes (CR and MB). Optimization calculations were performed with the PM7 semi-empirical method in an implicit solvent (water) using the COSMO [26] continuum model. In addition, all atoms of the palygorskite surface were constrained during the optimization process. The MOPAC 2016 software [27] program was used for the PM7 calculations using the MOZYME algorithm [28]. The PM7 method includes dispersion and hydrogen bonding correction terms, enabling to reliably describe various types of non-covalent interactions [29]. The PM7 method can indeed be suitable for adsorption studies involving larger systems [30], which are computationally demanding for DFT or *ab initio* methods.

Both dyes are charged species in aqueous solution at neutral pH. The CR dye tends to exist in its dianionic form because of its two sulfonic cores, while the MB dye has one positive charge which is delocalized in the aromatic system [31]. Therefore, some positions and orientations of the dye(s) on the palygorskite surface were tried to indicate the more favorable interaction structures for this adsorbate/adsorbent system. As shown in the Fig. 1, the charged atomic centers of the dye(s) were probed in the vertical (up and down) and horizontal orientations along the x and y directions. The adsorption enthalpy (ΔH_{abs}) was estimated according to the following expression: $\Delta H_{abs}=H_{absorbent/adsorbate}-(H_{absorbate}+H_{absorbent})$, where the $H_{absorbent}$ and $H_{absorbate}$ correspond to the formation enthalpy of the isolated absorbent (supercell of the palygorskite surface) and of the free absorbate(s) (CR and MB dyes), respectively, and $H_{absorbent/adsorbate}$ is the formation enthalpy of the absorbent/adsorbate system. The overall methodology employed in this research is presented in a simplified flow diagram depicted in Fig. 2.

RESULTS AND DISCUSSION

1. Adsorbent Characterization

The chemical composition of the palygorskite samples (Table 2) showed the major oxides constituents of Pal clay mineral before and after the acid activation. These results indicate a decrease in the percentage of some oxides as Al_2O_3, Fe_2O_3 and MgO due to the leaching process caused by the acid in the octahedral metallic cations of Pal structure [4,32].

The X-ray diffraction (XRD) patterns of Pal and APal with their respective refinements are depicted in Fig. 3. The experimental data

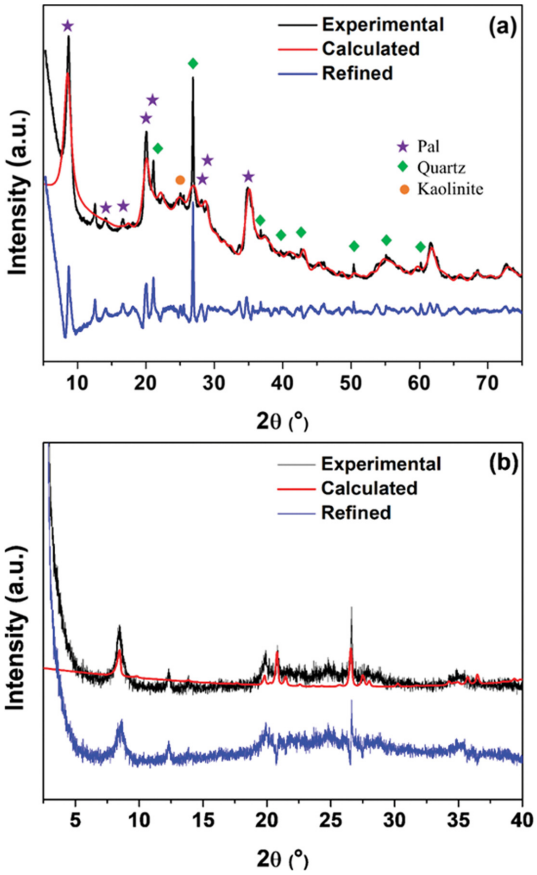

Fig. 3. XRD data for (a) Pal and (b) APal. The test was performed with copper radiation (CuKα, λ=1.54 Å), a 2θ range of 5° and 5-90°, step of 0.01°, a Ni filter, a current of 10 mA and voltage of 30 kV.

from raw Pal shows the main palygorskite peaks, with the main peak at 2θ=8.4° (COD ID 9005565), which corresponds to an interplanar distance (d_{hkl})=1.1 nm that can be attributed to the base plane of the palygorskite structure. Other characteristic peaks (2θ=14.04°, 16.64°, 19.92°, 21.10°, 28.14°, 28.92° and 34.91°) are also presented in its structure and correspond to the crystalline planes (110, 200, 130, 040, −221, 400, 221, respectively), confirming the presence of this clay mineral [31]. Other reflections are assigned to impurities such Quartz at 2θ=21.26° (COD ID 9011493), 26.91°, 36.77°, 42.65°, 50.41°, 55.12° and 60.19° [33,34] and the Kaolinite at 2θ=25.10° (COD ID 9009234). The main peaks continue to be seen in the spectrum after acid treatment, albeit with less intensity and with broader bases. Less intense peaks present in Pal disappeared after acid treatment. This effect occurs due to acid leaching which promotes the removal by dissolution of metals such as Mg^{2+}, Al^{3+} and Fe^{3+} located in the octahedral planes, as showed in the XRF data, which possibly generates a form of amorphous silicate when disso-

Table 2. Chemical composition of Pal and APal

Composition (%)	SiO_2	Al_2O_3	Fe_2O_3	MgO	K_2O	TiO_2	Others
Pal	58.99	15.70	12.45	4.70	2.10	1.18	1.24
APal	76.15	11.71	3.26	3.50	1.17	1.24	2.37

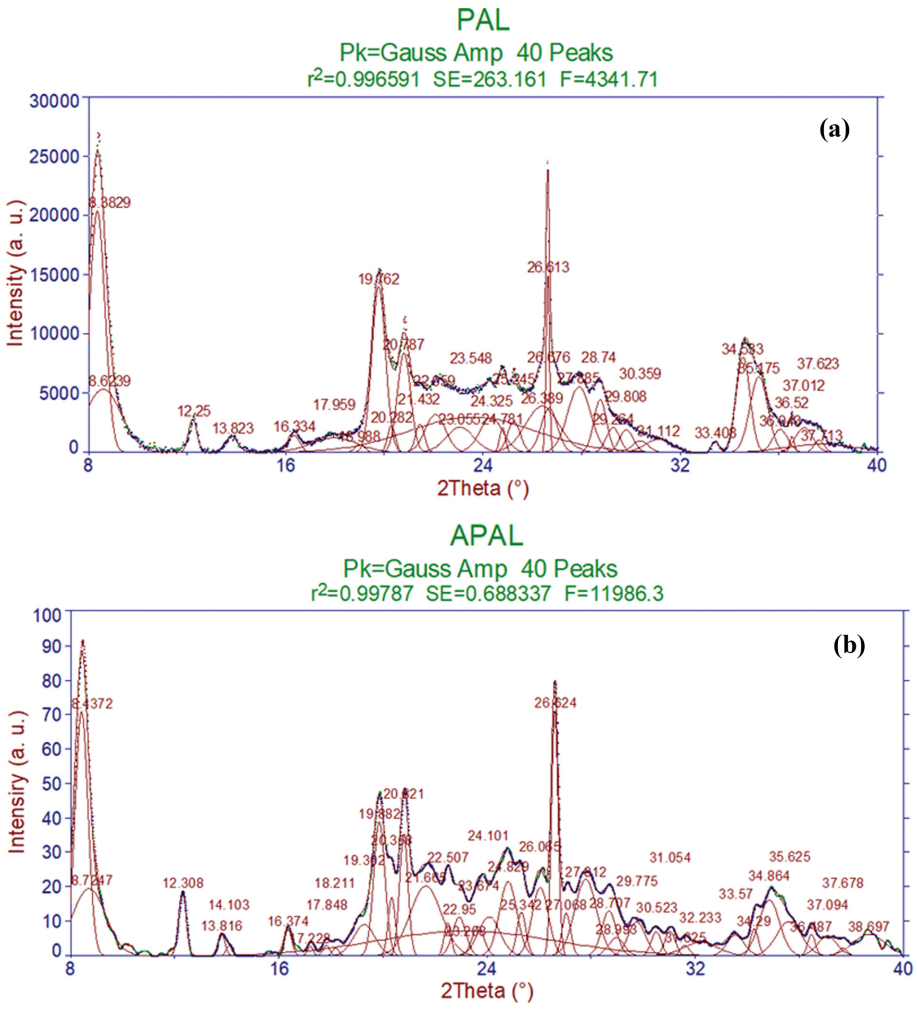

Fig. 4. XRD deconvolution for (a) Pal and (b) APal.

ciated that can be justified by the decrease in intensity and enlargement of the peaks [35].

The refinement presented 93.1% palygorskite, 5.9% quartz and 0.86% kaolinite for the natural Pal, whereas the result for the acid treatment sample was 43.7% palygorskite, 54.8% quartz and 1.3% kaolinite. Palygorskite has a complex chemical composition and presents a certain degree of amorphicity, which causes refinement results outside the expected standard for this technique. Extra refinement tests imply data distortion and loss of reliability of these data, so that the results obtained were the ones that best fit.

The adjustments show that natural palygorskite is composed of many mineral compounds. They are seen as interfering in this work since they have not been quantified, for example, dolomite and calcite [23]. Fig. 4 shows the XRD deconvolution models for Pal and APal.

The deconvoluted diffractogram for Pal shows the presence of an amorphous peak in 2θ=26.05°. By measuring the width of these peaks, it is possible to note that this sample presents an amorphous percentage of 16.65%. This percentage decreased to 14.04% after the acid treatment, indicating high crystallinity. These results also confirm those obtained by the Rietveld refinement with the reduction of palygorskite content after the modification.

The FTIR spectra of Pal and APal are presented in Fig. 5(a), (b) and summarized in Table S1 (S indicates the Supplementary Material I). Raw Pal presents a band in the 3,695 cm^{-1} region attributed to the Al-OH stretching vibration. The feature in the 3,613 cm^{-1} region corresponds to the stretch vibrations of the structural hydroxyl groups for (Fe-OH, Mg-OH) and (Al-OH, Mg-OH). The band in the 3,535 cm^{-1} is attributed to the stretching vibration of -Si-OH. The band in the region of 2,920 to 3,786 cm^{-1} and 1,648 cm^{-1} refers to stretching vibration of hydroxyl groups of the adsorbed water molecules and coordinated water in the channels, respectively. The band at 910 cm^{-1} was associated to Al-OH-Al flexion and presents a predominantly dioctahedral character of Pal, typical of clay minerals with high aluminium levels. The feature at 981 cm^{-1} is attributed to Si-O-Mg asymmetric elongation. The band at 795 cm^{-1} is attributed to the vibration of Si-O-Si groups [33,34,36]. The deformation bands of the hydroxyls bound to metals suffered a decrease in intensity or disappeared after the acid treatment (APal) due to acid leaching resulting from the alteration of the tetrahedral sheet of SiO_4 [39]. The characteristic bands of the palygorskite attributed to the O-Si-O vibrations had their intensity reduced by the acid treatment [37]. The intensity of the coordinated water decreases with acid treatment, due to the gradual dissolution of the OH bound

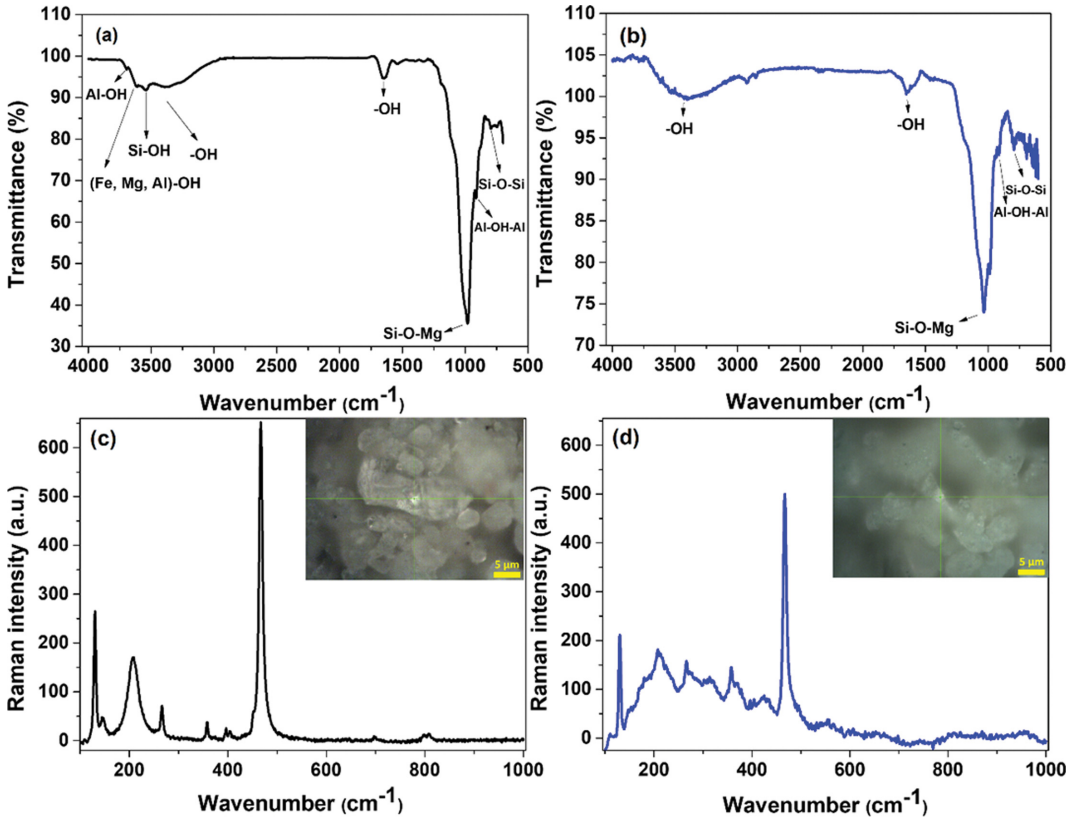

Fig. 5. FTIR spectra of (a) Pal and (b) APal and Raman spectra of (c) Pal and (d) APal. The FTIR spectra were obtained in the range of 700-4,000 cm^{-1} (4 cm^{-1} resolution and 32 scans). Raman spectra of the adsorbents were obtained employing 758 nm line of an Argon laser.

to the octahedral MgO at the edges of the channels, indicating the destruction of the octahedral sheet in the crystal structure of Pal. This can also be confirmed by the decrease in the intensity of the bending vibration of the Al-OH-Al deformation band by 910 cm^{-1} [38].

The results obtained by Raman spectroscopy allowed us to identify the main species of magnesium and silicate species present in the clay mineral structure. All samples were tested under low laser power (25%) to avoid decomposition. As depicted in Fig. 5(c), (d), the adsorbents display a band at 130 cm^{-1} corresponding to the silicate tetrahedral ring deformation. The three peaks at 170, 206 and 267 cm^{-1} indicate the O-Mg-O bend, the silicate sheet deformation with the SiO_4 rotation and the Mg octahedral deformation, respectively. The peaks at 356, 405 and 470 cm^{-1} can be attributed to the Si-O formation, the Si-O-Si bend and MgO_6 octahedral rotation. The Raman microscopy images showed a crystal agglomerate structure with fibrous shape [39].

FESEM micrographs for Pal and APal are presented in Fig. 6, showing that this clay mineral presents the characteristic morphology of the palygorskite in fibrous shape with agglomerate structures in the form of ribbons, needles or canes with varying dimensions [34]. The mapping images (Fig. 6(b)-(g)) indicate a dispersion of the elements O, Si, Al, Fe, Mg and K, and EDX spectrum, with Fig. 6(h) showing its elemental composition. EDX measurements are generally used to confirm the percentage, the atomic ratio, of the component types on the surface of the materials [40]. Non-fibrous agglomerates and agglomerates with fibrous traces are observed after the acid treatment (APal) (Fig. 6(i)), which is due to the acid treatment process that dissolved tetrahedral leaves of Pal and transformed in fibrous amorphous silica [41]. The mapping images (Fig. 6(j)-(p)) indicate that there is still dispersion of the elements in Pal and the results of the EDX spectrum (Fig. 6(q)) show that the Si and O elements had their percentages increased, while the Al, Fe, Mg and K elements had their percentages decreased due to acid leaching, agreeing with the data obtained previously in XRF.

The N_2 adsorption-desorption isotherms performed before and after Palygorskite modification are shown in Fig. 7, as well as the pore size distribution plot, while Table 3 contains the textural parameters. According to the IUPAC classification, the Pal and APal isotherms can be considered as type IV, with H3 hysteresis loops which are characteristic of mesoporous structure and show that adsorbents have slit-shaped pores which come from aggregation in chape plate-like particles [42]. An increase in the specific area (S_{BET}) value occurs after the acid treatment due to the aperture of the structural

Table 3. Textural properties of Pal and APal

Adsorbent	S_{BET} [a] (m^2/g)	V_P [b] (cm^3/g)	Pore diameter (Å)
Pal	106	0.41	37.62
APal	180	0.63	34.72

[a]Specific surface area by Brunauer-Emmett-Teller (BET) method.
[b]Total pore volume in p/p_0=0.996 (0.985).

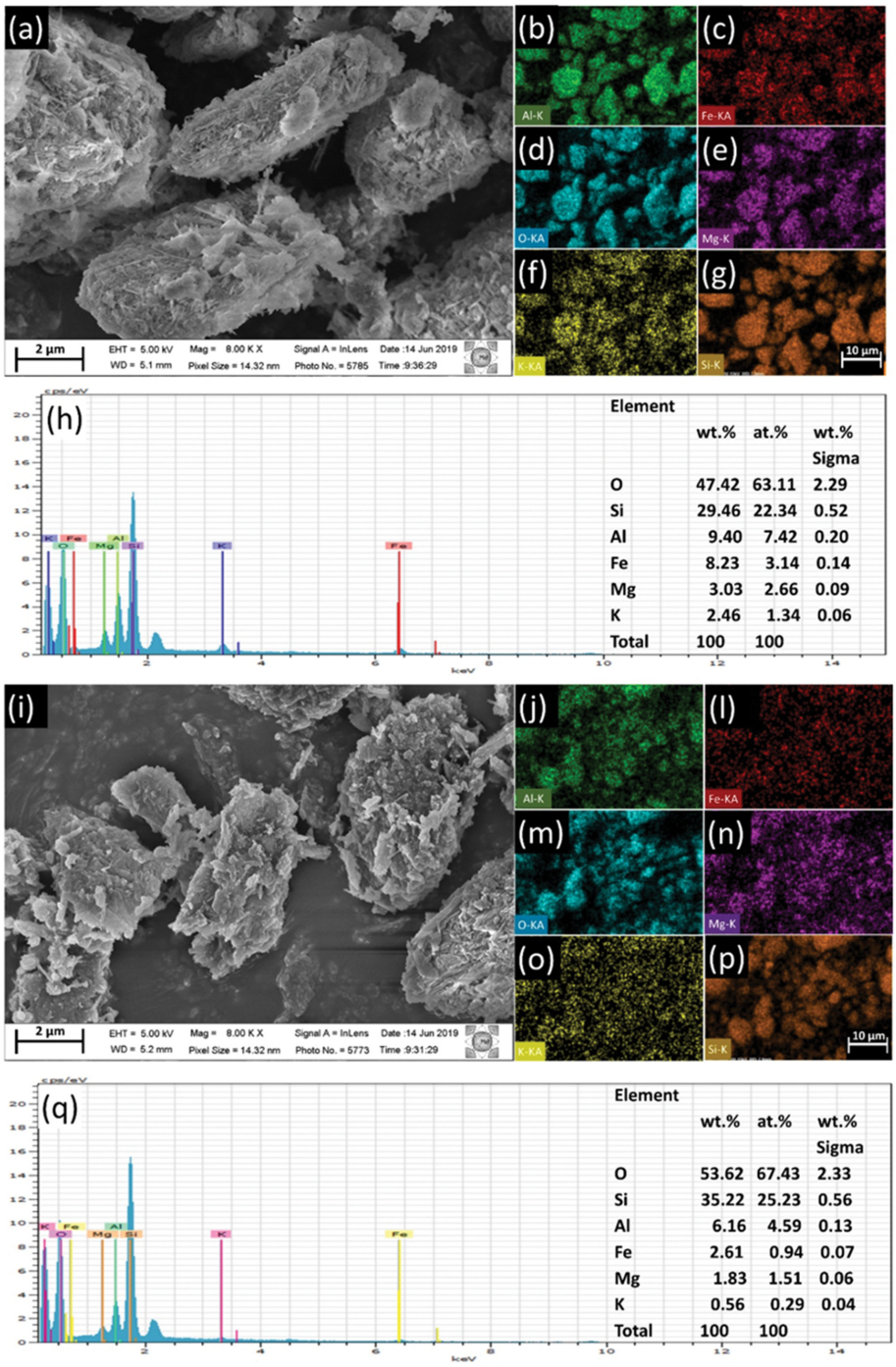

Fig. 6. (a) FESEM; (b)-(g) mapping images and (h) EDX spectrum for Pal. (i) FESEM; (j)-(p) mapping images and (q) EDX spectrum for APal.

channels after dissolution of the octahedral sheet and the shaping of amorphous silica and dissolution of the octahedral cations. The increase in pore volume would be associated with mesoporosity [37]. The decrease in pore diameter implies that APal pores change in comparison to Pal, and this may be associated with a greater growth in percentage of micropores than mesopores due to acid treatment [43]. The modification in the pore diameter can be seen in the pore size distribution curve in Fig. 7.

X-ray photoelectron spectroscopy (XPS) analysis was used to determine the elemental composition of the valence states of chemical compounds. The XPS survey spectra from Pal are presented in Fig. 8. The results show the presence of peaks for Si, O, Mg, Al, K and Fe elements. Peak C 1s can be attributed to the carbon of the instrument itself [42]. The photo emissions of the 102.8 eV, 532.0 eV, 50.3 eV, 74.5 eV, 293.2 eV and 712.8 eV peaks correspond to the binding energy (BE) states of Si 2*p*, O 1*s*, Mg 2*p*, Al 2*p*, K $2p_{3/2}$

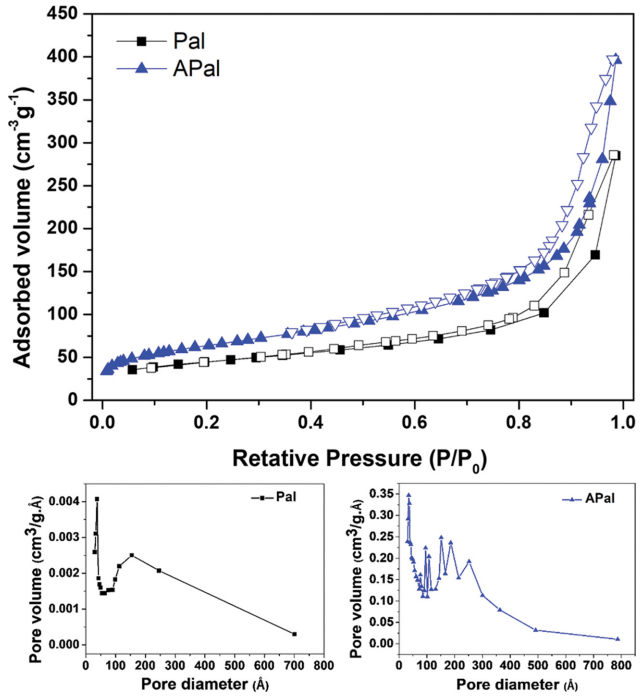

Fig. 7. N_2 adsorption-desorption isotherms at 77 K and BJH adsorption pore size distributions Pal and APal.

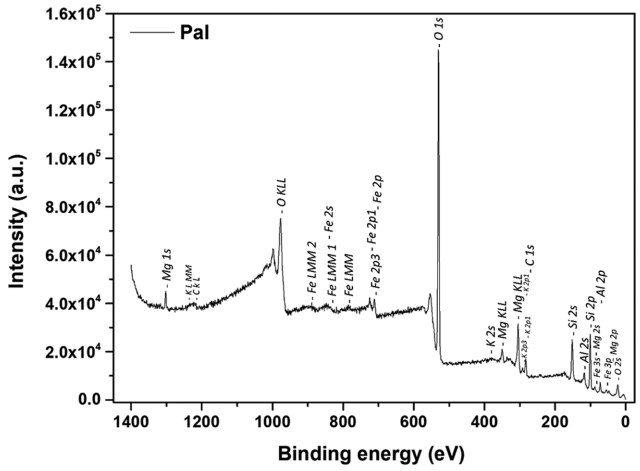

Fig. 8. XPS spectra for Pal. The tests were carried out using a Non-monochromatic Al Kα radiation (95.2 W, 15 kV, and 1,486.6 eV).

and Fe $2p_{3/2}$, respectively [44].

2. Adsorption Study

2-1. Adsorption Kinetics

The effect of contact data (depicted in Fig. 9) shows that the initial adsorption rate of MB dye in aqueous solution onto Pal or APal surface and in the binary mixture (50% MB+50% CR) on Pal was fast in the first 5 minutes, followed by a reduction in velocity until reaching equilibrium. The amount of adsorbed CR dye in aqueous solution over Pal or APal surface (Fig. 9(a)) was rapid in the first 30 min, followed by a slower rate. The balance for the adsorption of dyes in the binary systems was established in about 60

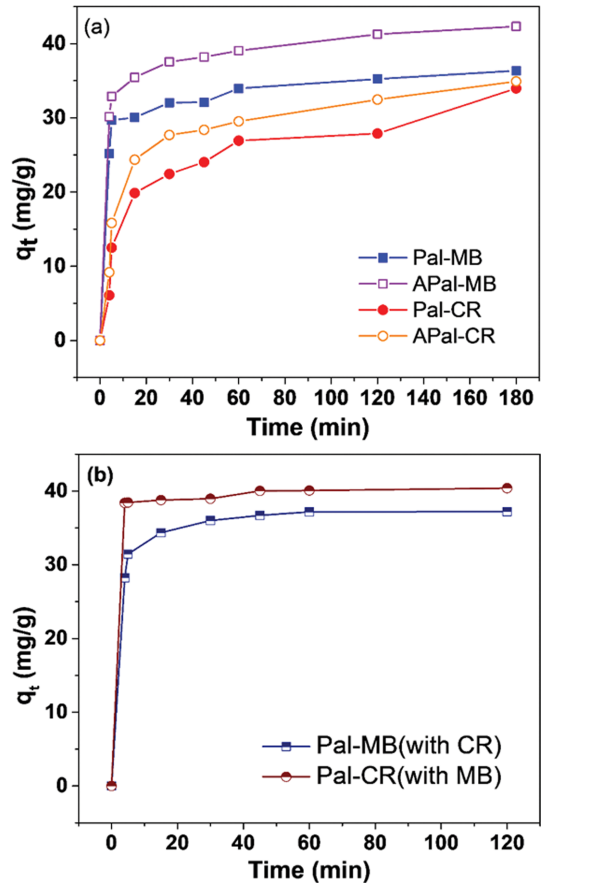

Fig. 9. Effect of the contact time of the adsorption of MB and CR dyes on palygorskite (natural or acidic) in single (a) and binary (b) systems.

min, while the balance was not clearly achieved for the adsorption in single systems. The amount adsorbed quickly in the first stage can be attributed to the availability of reaction sites on the clay surface, while the subsequent slow stages are due to saturation of the reaction sites by the dyes, implying a reduction in the adsorption efficiency [45,46]. The adsorption capacity of the dyes by the acid-treated palygorskite was greater at the studied time interval than by the natural palygorskite (Fig. 9(a)).

The mathematical models of pseudo-first-order, pseudo-second-order, Elovich, intraparticle diffusion and Boyd film diffusion were used to investigate the adsorption mechanisms. The experimental data were adjusted to the kinetic models and the results are recorded in Fig. 10((a), (b), (c), (d) and (e)) and Table 4. The R^2 values for the pseudo-second-order ($1>R^2>0.98$) were higher than those obtained by the pseudo-first-order equation ($0.98>R^2>0.77$). In addition, the theoretical and experimental q_e values estimated by the pseudo-first order model were substantially different, while those estimated by the pseudo-second-order model were similar.

Thus, the experimental results were better adjusted by the pseudo-second-order kinetic model, suggesting that the chemisorption process is the determining step in the adsorption rate of MB and CR dyes in aqueous solution over natural or acid-activated palygorskite and binary mixture (50% MB+50% CR) on natural palygor-

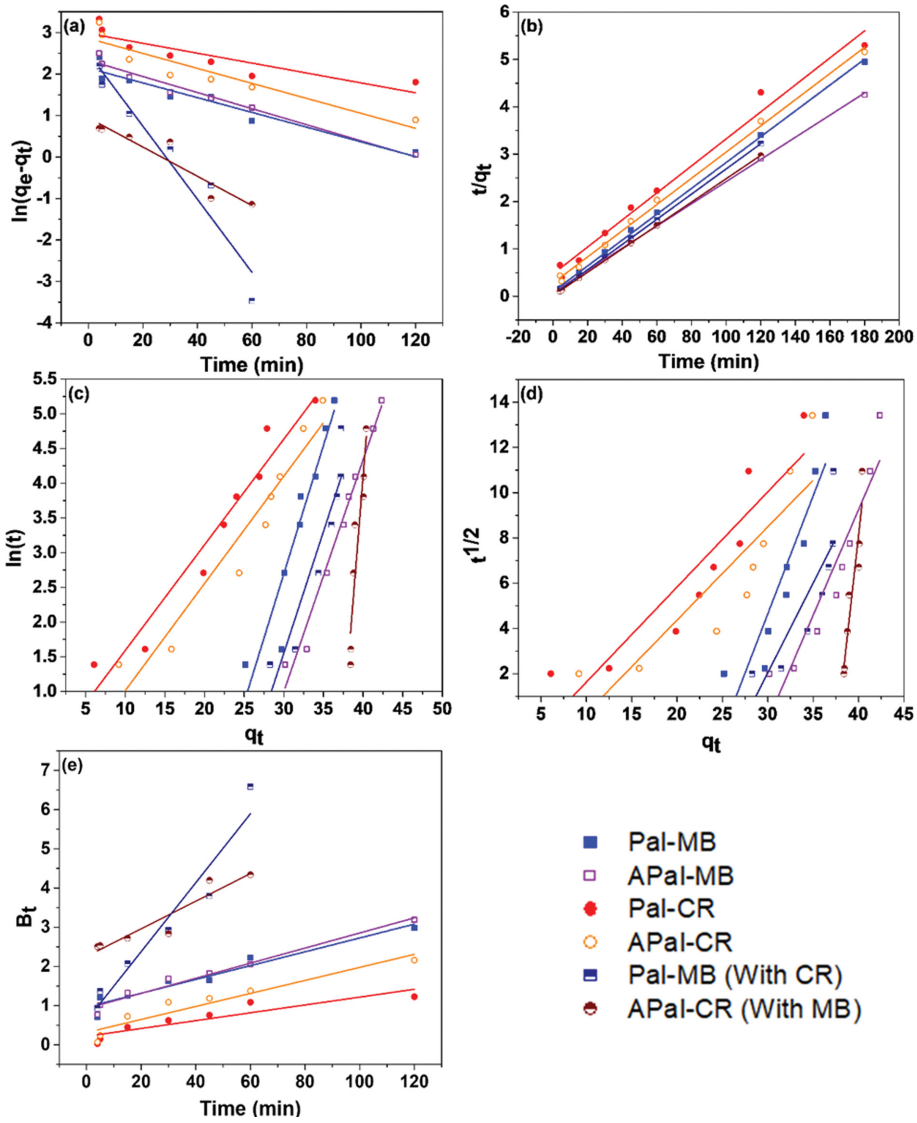

Fig. 10. Fitting curves of (a) pseudo-first-order, (b) pseudo-second-order, (c) Elovich, (d) intraparticle diffusion and (e) Boyd kinetic models.

skite under the evaluated conditions [47]. After acid treatment, an increase was observed in the amount of dyes adsorbed ($q_{e,cal}$) since some impurities were removed from the clay mineral surface, resulting in the increase in its pore volume and surface area (Table 3), due to leaching process that changes the octahedral cations in Pal and, possibly influenced in the adsorption kinetic. The increase in the adsorption capacity of the dyes in binary systems is an indication that there was no competition between the adsorbates, since the cationic (MB) and anionic (CR) dyes do not compete for the same reaction sites on the clay surface, but rather a synergistic effect with a strong interaction between them [45]. The adsorption data was fitted to the Elovich kinetic model ($0.88<R^2<0.98$), reinforcing that chemical adsorption governs the studied adsorptive process.

The intraparticle and Boyd diffusion models were used to investigate the adsorption processes limiting step. The intraparticle diffusion model curves were generally linear and did not pass through the origin (Fig. S1), which indicates that intraporous diffusion is not the only rate control factor. The C_i values shown in Table 4 reveal that the effects of the boundary layer were greater for the MB adsorption in a single system and of MB and CR in the binary mixture. Although the Boyd model graphs (Fig. S1) exhibit good linearity ($0.83<R^2<0.98$), they do not intersect at the origin, suggesting that the diffusion of pores is not the rate controlling step and that there is a resistance step for the mass transfer in the external film [48].

2-2. Adsorption Equilibrium Studies

The Langmuir, Freundlich and Temkin isotherm models were used to evaluate the experimental adsorption data. The parameters obtained and correlation coefficients (R^2) are listed in Table 5. The linear and nonlinear fits of the adsorption results are shown in Fig. 11 and S1, respectively. The linear equation for each Langmuir and Freundlich isotherms model with the experimental data is depicted in Fig. S2 and S3, respectively. The three models were well suited to the experimental data ($R^2>0.91$) based on the R^2 values; however, the Langmuir model provided the best fit with R^2 values closer to 1, which suggests that the studied adsorbent pro-

Table 4. Parameters for the fitting to pseudo-first-order, pseudo-second-order, intraparticle diffusion, Boyd film diffusion and Elovich models of dye adsorption on Pal and APal

Kinetic parameters	Pal-MB	APal-MB	Pal-CR	APal-CR	Simultaneous adsorption	
					MB	CR
$q_{e,exp}$ (mg/g)	36.362	42.331	33.975	34.917	37.214	40.403
Pseudo-first-order						
k_1 (min^{-1})	−0.018	−0.019	−0.012	−0.018	−0.088	−0.035
$q_{e,cal}$ (mg/g)	8.530	10.294	19.725	17.471	12.262	2.575
R^2	0.9331	0.9713	0.7742	0.8694	0.9388	0.8938
Pseudo-second-order						
k_2 (g/mg min)	0.008	0.007	0.002	0.003	0.022	0.043
$q_{e,cal}$ (mg/g)	36.637	42.731	35.094	36.103	37.590	40.484
R^2	0.9991	0.9993	0.9845	0.9975	0.9999	0.9999
Elovich						
α (mg/g min)	5.04×10^{-11}	6.19×10^{-13}	2.37×10^{-1}	4.89×10^{-3}	2.74×10^{-12}	1.08×10^{-16}
β (g/mg)	2.702	2.991	6.566	6.472	2.851	0.705
R^2	0.9016	0.9792	0.9498	0.9301	0.8849	0.8828
Intraparticle diffusion						
k_{id} (mg/g $min^{1/2}$)	0.803	0.955	2.015	1.878	0.899	0.249
C_i (mg/g)	26.573	30.850	8.518	12.984	29.445	37.910
R^2	0.8374	0.8902	0.8473	0.7742	0.7123	0.9006
Boyd						
B	0.018	0.019	0.010	0.017	0.088	0.035
R^2	0.9369	0.9736	0.8352	0.9125	0.9385	0.8938

Table 5. Parameters for the fitting of dye adsorption onto Pal and APal for the Langmuir, Freundlich and Temkin models

Isotherm parameters	Pal-MB	APal-MB	Pal-CR	APal-CR
Langmuir				
q_m (mg/g)	11.302	120.480	2.731	238.095
$K_L\times10^3$ (L/mg)	2.081	8.536	8.042	1.134
R_L	0.493	0.190	0.204	0.642
R^2	0.9994	0.9743	0.9978	0.9755
Freundlich				
N	1.201	1.560	1.764	1.281
K_F (L/g)	0.039	2.630	0.077	0.599
R^2	0.9978	0.9215	0.9884	0.9601
Temkin				
α (L/g)	0.045	0.108	0.074	0.055
β (J/mol)	1.720	26.294	0.641	17.581
R^2	0.9354	0.9194	0.9859	0.9637

cess occurs by the material surface saturation due to the formation of a monolayer [49]. In addition, the best fit of the data by this mathematical model implies that the adsorption rate is controlled by chemical processes, which is in line with the results of the kinetic models [50]. The calculated R_L values ($0<R_L<1$) reflect the favorable adsorption of MB and CR on Pal or APal surface. This is confirmed by the values of n between 1 and 10.

The significant increase in the maximum Langmuir adsorptive capacity (q_m) and in the Freundlich adsorptive capacity (K_F) for the acid-activated palygorskite indicates that this modification generated a considerable number of adsorption sites. This hypothesis is also supported by the increase in the specific area of the clay after the acid treatment (as shown in Table 3), which was expected since the acid activation causes the replacement of exchangeable cations by H^+ ions with the simultaneous loss of ions Al^{3+}, in addition to other cations of the tetrahedral and octahedral layers, leaving the SiO_4 groups intact [51].

2-3. Comparison of Research Findings

Palygorskite and acid-treated palygorskite used to remove methylene blue and Congo red dyes in this study were compared with some adsorbents described in the literature. In Table 6, it can be seen that Pal and APal present similar or higher adsorption capac-

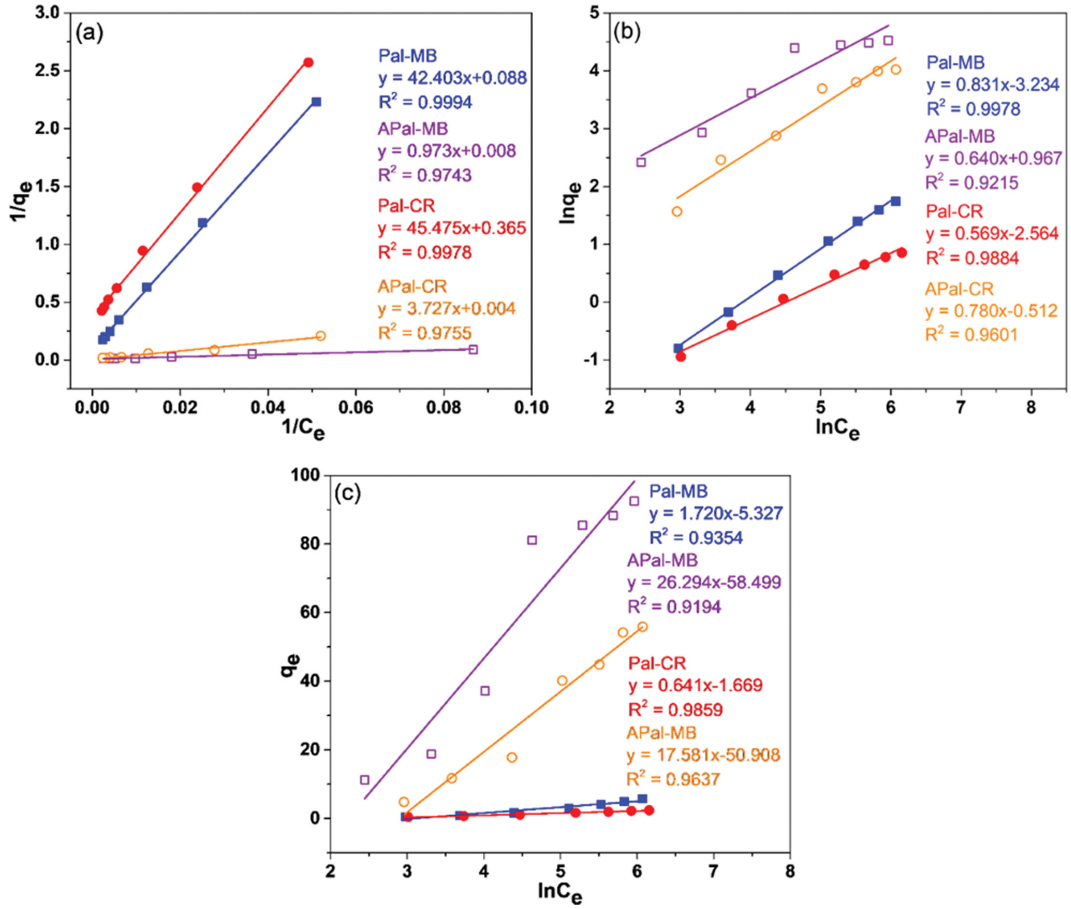

Fig. 11. Linear isotherm plots of (a) Langmuir, (b) Freundlich and (c) Temkin.

Table 6. Comparison of research findings in MB and CR dye adsorption

Adsorbent	Dye	q_m (mg/g)	Reference
Kaolinite (Algeria)	MB	52.7	[52]
Natural clay (Portugal)	MB	22.2	[53]
Palygorskite Guanshan (GSHN)	MB	98.34	[18]
Palygorskite (APTES)	MB/MY*	49.48	[14]
Amines functionalized palygorskite	MB	13.6	[54]
Magnesite-halloysite nanocomposite	MB	0.7	[55]
Ca-Pal	MB	57.47	[3]
Acid-treated Ca-Pal	MB	96.15	[3]
Palygorskite	MB	11.3	This paper
Acid-treated palygorskite	MB	120.4	This paper
$Fe_XCo_{3-X}O_4$ nanoparticles	CR	50.8	[56]
Activated carbon	CR	63.4	[57]
Leonardite	CR	61.7	[58]
Hydroxyapatite nanoparticle	CR	72.9	[59]
Palygorskite	CR	2.7	This paper
Acid-treated palygorskite	CR	238.1	This paper

*MY: Metanil yellow.

ity compared to the other material adsorbents, which can occur due to small variations in palygorskite richness and/or in fiber dimensions [3]. This higher adsorption capacity onto Pal surfaces is attractive for its use as an adsorbent material for dye removal in aqueous solutions since clay and clay mineral materials are low-cost and abundant in nature. Furthermore, no additional preparation or syn-

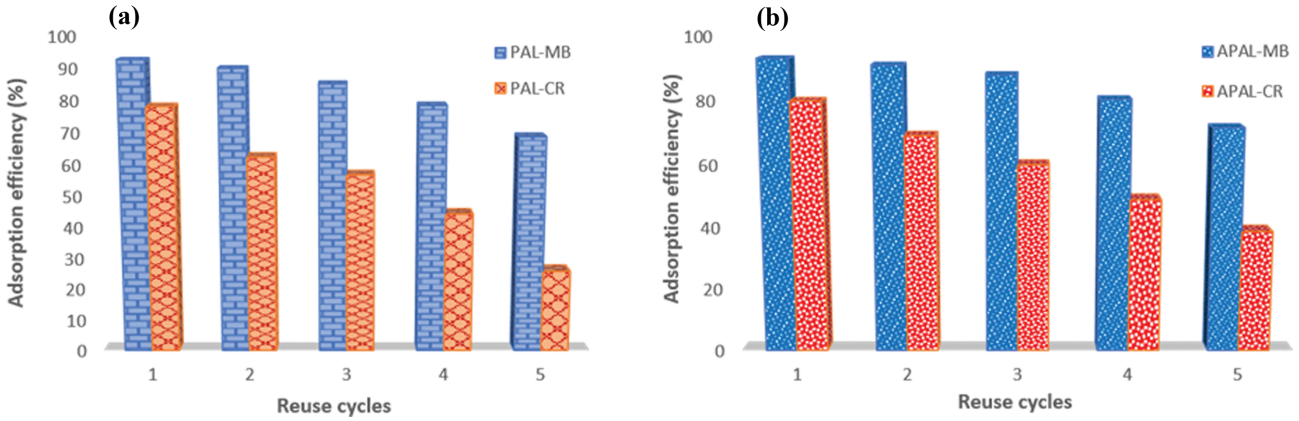

Fig. 12. Dye adsorption results for the regenerated materials (a) Pal and (b) APal.

thesis processes are necessary.

2-4. Desorption and Regeneration Studies

Regeneration is one of the most significant aspects in adsorption study, to make the process more economical and environmental-friendly. The recovery test was repeated for five cycles and the results are depicted in Fig. 12. The adsorbents presented a satisfactory reuse rate for both dyes with the adsorption capacity decreasing for every new cycle, indicating that the methodology was successful in removing dyes in aqueous solutions without compromising their adsorption efficiency.

3. Computational Study

Semi-empirical calculations were performed to better understand the adsorbate/adsorbent interaction system between the palygorskite clay and the commercial dyes (MB and CR). Thus, optimization calculations were carried out by scanning some positions and orientations of the dye(s) on the palygorskite surface to indicate possible binding types for the adsorbate/adsorbent system. As can be observed in Table 7, the obtained adsorption enthalpy (ΔH_{abs}) values are favorable for all cases. The calculated values for the ΔH_{abs} for the CR/palygorskite system are in the range from −189.1 to −47.7 kJ/mol, whereas the calculated values for the MB/palygorskite system range from −142.2 to −1.3 kJ/mol. The adsorption enthalpy for chemical adsorption typically ranges from −40 to −800 kJ/mol, while the physical adsorption processes range from −4 to −40 kJ/mol [60]. Thus, the calculated ΔH_{abs} values suggest that the adsorption process between the palygorskite surface and the dyes (MB and CR) might be considered as chemical adsorption.

The obtained results generally suggest that the palygorskite surface interacts more strongly with CR dianionic dye than with the MB cationic dye (see Table 7). Although both dyes are aromatic systems, the CR dye has conformational flexibility due the simple bonds between the biphenyl, azo, and aminonaphthalenesulfonic groups. This enables the CR dye to enhance the attractive supramolecular interactions with the irregular and discontinuous palygorskite surface. The optimization calculations point out that the CR molecule tends to spread out more on the palygorskite surface compared to the MB species [61]. In contrast, the MB molecule maintains its planar geometry when adsorbed on the palygorskite surface. A theoretical study has also identified that the molecular geometry of the MB is basically unaltered when adsorbed onto the surface of Ag and Au metals [62].

The calculations also indicate that the CR and MB dyes appear to have different adsorption modes on the palygorskite surface. The most favorable results for the CR dye are obtained along the y direction, while the x direction is enthalpically more favorable for the MB dye (see Table 7). In addition, each dye appears to interact with the palygorskite surface through different types of binding sites. Fig. 13 displays the most energetically favorable structures obtained for the interaction between the dyes (MB and CR) and the surface. On the one hand, the CR/palygorskite system is driven by strong hydrogen bonds: (i) between the sulfonic core (dye) and OH_2 molecules (which coordinate the Mg ion in the zeolitic channels); (ii) and/or between the hydrogens of the amino groups (dye) and the surface oxygen atoms (which coordinate the metallic centers). On the other hand, the MB/palygorskite system is mediated by a strong ion-dipole interaction between the S atomic center (dye) and the surface oxygen atom (which coordinate the metallic centers). Indeed, the most exothermic ΔH_{abs} (u_x and h_y in the Table 8) for the MB/palygorskite system occurred when the bonding distances between the S (dye) and O (from the surface) atoms were ca. 1.73 Å.

Table 7. ΔH_{abs} (in kJ/mol) were calculated using the PM7 method. The $u_{x,y}$ (up), $d_{x,y}$ (down), and $h_{x,y}$ (horizontal) notations represent orientations of the dyes on the palygorskite surface along the x and y directions (see Fig. 1)

Dyes	d_x	d_y	h_x	h_y	u_x	u_y
CR	−69.0	−189.1	−47.7	−84.1	−89.5	−154.8
MB	−28.0	−1.3	−44.8	−142.2	−125.9	−33.9

Table 8. Calculated ΔH_{abs} (kJ/mol) for the simultaneous absorption of the two dyes. Vertical (down, d) and horizontal (h) orientations are selected for the CR and MB dyes, respectively, along the x and y directions (see Fig. 1)

	MB/CR orientations			
	h_x/d_x	h_x/d_y	h_y/d_x	h_y/d_y
Adjacent cavities	−113.8	−150.2	−134.7	−298.7
Same cavity	−167.1	−84.5	−156.9	−149.8

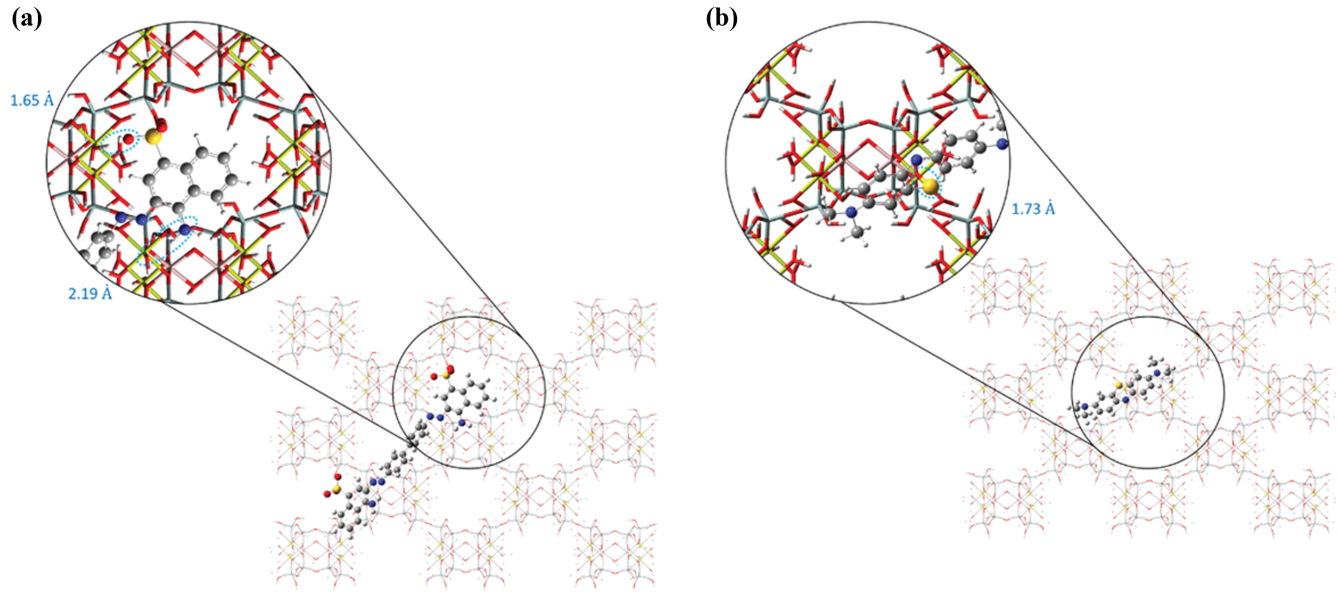

Fig. 13. Structural points calculated with the PM7 method for the adsorption of (a) CR and (b) MB (with d_y and h_y orientations, respectively) on the palygorskite surface. The surface is represented in wireframe form. Relevant binding sites and bond distances (Å) are displayed in ball-and-stick forms. The coloring scheme of the atoms is the same as in Fig. 1.

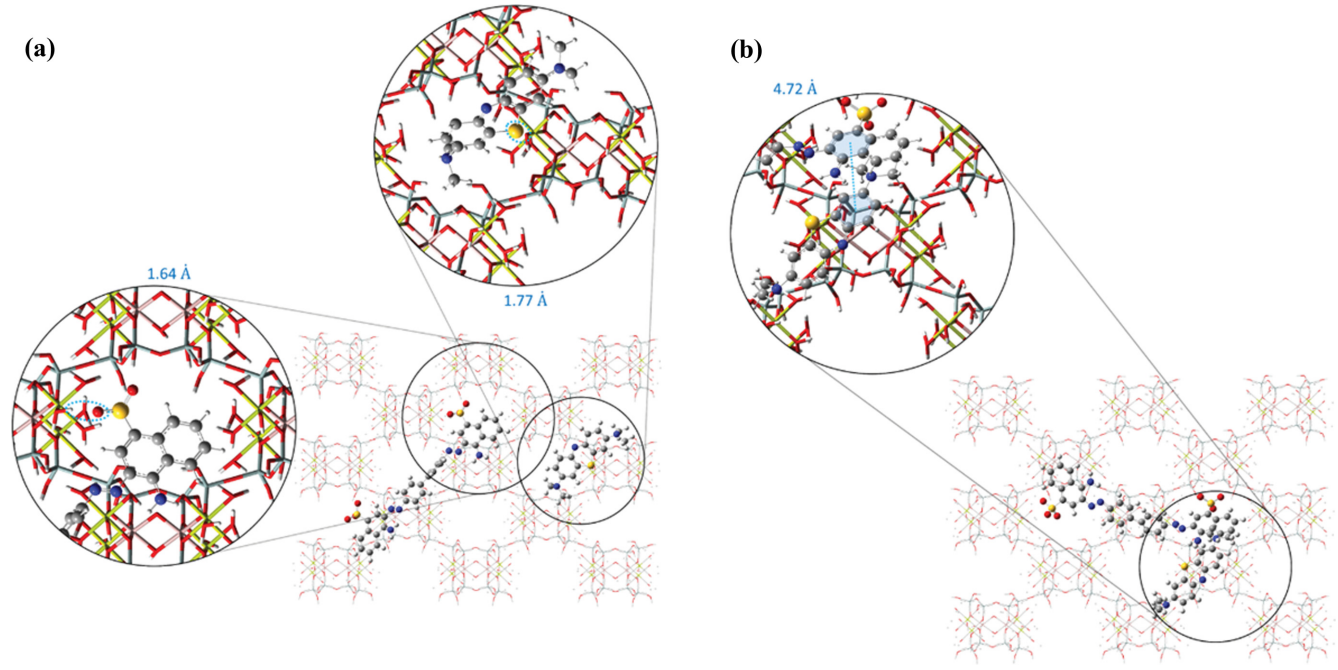

Fig. 14. Structural points calculated with the PM7 method for the simultaneous absorption of the two dyes on the palygorskite surface. (a) and (b) represent the adjacent and same zeolitic cavities with the h_y/d_y and h_x/d_x orientation for MB/CR, respectively. The surface is represented in wireframe form. Relevant binding sites and bond distances (Å) are displayed in ball-and-stick forms. In Part (b), the calculated distance between the aromatic centroids is 4.72 Å. The coloring scheme of the atoms is the same as in Fig. 1.

ΔH_{abs} calculations were also performed to assess the capacity of the palygorskite clay to simultaneously adsorb the two dyes. Thus, the CR and MB dyes were selected in the d and h orientations, respectively. In addition, the dyes were probed along the x and y directions, considering them at adjacent zeolitic cavities and also sharing the same cavity. As shown in Table 8, the obtained ΔH_{abs} values (ranging from −298.7 to −84.5 kJ/mol) indicate that the two dyes can interact strongly with the palygorskite surface.

Fig. 14 shows two structures obtained for the interaction of the dyes in binary system with the palygorskite surface. Videos showing these molecular interactions using PM7 model simulation are included in Supplementary Material II (ES3_A, ES3_B and ES3_C).

As already observed from the calculations with the individual species, each dye does not appear to compete by the same interaction site on the palygorskite surface (see Fig. 14(a)). Furthermore, the calculated structures point out that the dyes can effectively share the same cavity on the palygorskite surface. As can inferred from Fig. 14(b), the aromatic dyes appear to have a synergistic effect through effective π-π stacking [63].

CONCLUSION

The results of XRF data provided a decrease in the concentration of some metal oxides, such as Fe_2O_3, Al_2O_3 and MgO, due to the leaching caused by the acid treatment. The results of XRD and refining show that Pal has impurities such as quartz and kaolinite in small proportions, representing 5.90% and 0.86% of the sample, respectively. FESEM micrographs show that after acid treatment the tetrahedral sheets of Pal dissolved into amorphous silica, being consistent with the chemical analysis that showed that acid leaching occurs with acid treatment, perceived by the decrease in the percentage of most octahedral metallic cations present in palygorskite.

The application of computational tools associated with equilibrium and kinetic models for adsorption of ionic dyes in aqueous effluents using Pal appears in this work as a promising process for removal of pollutants of environmental systems. The application of computational tools associated with equilibrium and kinetic models for adsorption of ionic dyes in aqueous effluents using Pal appears in this work as a promising process for removal of pollutants of environmental systems. The adsorption data was fitted to the pseudo-second-order kinetic model, and presented a q_{exp} very close to the q_{cal}, suggesting that the chemisorption process is the determining step in the adsorption rate of MB and CR dyes in aqueous solution over natural or acid-activated palygorskite and binary mixture (50% MB+50% CR) on natural palygorskite under the evaluated conditions and Langmuir, with a q_m=120.8 mg·g^{-1} for APal-MB and q_m=238.1 mg·g^{-1} for APal-CR, which suggests that the studied adsorptive process occurs due to the saturation of the material surface due to the formation of a monolayer and that the adsorption rate is controlled by chemisorption; this is in agreement with the results of the kinetic models. The increase in the adsorption capacity of dyes in binary systems indicated a synergistic effect with a strong interaction between them.

Semi-empirical calculations using PM7 method suggest that the palygorskite surface can interact strongly with both dyes (separately or simultaneously) from different types of binding sites. Theoretical results indicated that the CR dianionic dye tends to spread out more on the surface compared to MB cationic dye to enhance the favorable supramolecular interactions. In contrast, the MB dye maintains its planar geometry and the MB/palygorskite system is driven by a strong ion-dipole interaction between the surface oxygen atom and the S atomic center (dye).

Palygorskite stands out in this paper as adsorbent of dyes in aqueous solution for being eco-friendly, abundant in nature and, due to its specifical composition and properties, proven by different characterization methods. Furthermore, the adsorbents presented a satisfactory regeneration rate.

ACKNOWLEDGEMENTS

The authors acknowledge the support provided by the Post-Graduate Chemistry Program (PPGQ/UFRN), the Energetic Technologies Research Group, and the Central Analitica (IQ/UFRN) and to the High-Performance Computing Center at UFRN (NPAD/UFRN). This study was partly financed by the Coordenação de Aperfeiçoamento de Pessoal de Nível Superior - Brasil (CAPES) - Finance Code 001.

COMPETING INTERESTS

There are no conflicts to declare.

SUPPORTING INFORMATION

Additional information as noted in the text. This information is available via the Internet at http://www.springer.com/chemistry/journal/11814.

REFERENCES

1. M. Divriklioglu, S. T. Akar and T. Akar, *Environ. Sci. Pollut. R.*, **26**, 25834 (2019).
2. G. Crini, G. Torri, E. Lichtfouse, G. Z. Kyzas, L. D. Wilson and N. Morin-Crini, *Environ. Chem. Lett.*, **17**, 1645 (2019).
3. L. D. Youcef, L. S. Belaroui and A. Lópes-Galindo, *Appl. Clay Sci.*, **179**, 105145 (2019).
4. A. K. Prajapati and M. K. Mondal, *J. Mol. Liq.*, **307**, 112949 (2020).
5. A. S. Eltaweil, G. S. Elgarhym, G. M. El-Subruiti and A. M. Omer, *Int. J. Biol. Macromol.*, **154**, 307 (2020).
6. Z. Li, H. Hanafy, L. Zhang, L. Sellaoui, M. S. Netto, M. L. S. Oliveira, M. K. Seliem, G. L. Dotto, A. Bonilla-Petriciolet and Q. Li, *Chem. Engineer. J.*, **388**, 124263 (2020).
7. J. N. Wekoye, W. C. Wanyonyi, P. T. Wangila and M. K. Tonui, *Environ. Chem. Ecotoxicol.*, **2**, 24 (2020).
8. T. A. Saleh, A. M. Elsharif and O. A. Bin-Dahman, *J. Mol. Liq.*, **340**, 117024 (2021).
9. A. A. Basaleh, M. H. Al-Malack and T. A. Saleh, *J. Environ. Chem. Eng.*, **9**, 105126 (2021).
10. I. Chaari, E. Fakfakh, M. Medhioub and F. Jamoussi, *J. Mol. Struc.*, **1179**, 672 (2019).
11. P. R. Souza, G. L. Dotto and N. P. G. Salau, *J. Environ. Chem. Engineer.*, **7**, 102891 (2019).
12. J. Pan, R. Li, L. Zhai, Z. Zhang, J. Ma and H. Liu, *J. Clean. Prod.*, **217**, 371 (2019).
13. U. Zhang, W. Wang, J. Zhang, P. Liu and A. Wang, *Chem. Eng. J.*, **263**, 390 (2015).
14. M. A. Moreira, K. J. Ciuffi, V. Rives, M. A. Vicente, R. Trujillano, A. Gil, S. A. Korili and E. H. Faria, *Appl. Clay Sci.*, **135**, 394 (2017).
15. G. Qiu, Q. Xie, H. Liu, T. Chen, J. Xie and H. Li, *Appl. Clay Sci.*, **118**, 107 (2015).
16. F. Zha, W. Huang, J. Wang, Y. Chang, J. Ding and J. Ma, *Chem. Eng. J.*, **215**, 579 (2013).
17. A. Middea T. L. A. P. Fernandes, R. Neumann, O. F. M. Gomes and L. S. Spinelli, *Appl. Surf. Sci.*, **282**, 253 (2013).

18. W. Li, J. Liu, J. Su, J. Wu, Y. Xia, L. Zhu, Z. Xu, W. Zhao, Y. Yan and D. Zhang, *J. Clean. Prod.*, **226**, 781 (2019).
19. H. M. Rietveld, *Acta Crystallogy.*, **22**, 151 (1967).
20. A. E. S. Choi, S. Roces, N. Dugos, A. Arcega and M. Wei Wan, *J. Clean. Prod.*, **161**, 267 (2017).
21. K. S. Tong, M. J. Kassin and A. Azraa, *Chem. Eng. J.*, **170**, 145 (2011).
22. F. Raganati, M. Alfe, V. Gargiulo, R. Chirone and P. Ammendola, *Chem. Eng. J.*, **372**, 526 (2019).
23. A. Habibi, L. S. Belaroui, A. Bengueddach, A. L. Galindo, C. I. S. Díaz and A. Peña, *Micropor. Mesopor. Mater.*, **268**, 293 (2018).
24. S. Spicher and S. Grimme, *Angew. Chem. Int. Ed.*, **59**, 2 (2020).
25. A. Klamt and G. Schüürmann, *J. Chem. Soc., Perkin Trans*, **2**, 799 (1993).
26. J. P. Stewart, MOPAC2016, Stewart Computational Chemistry, Colorado Springs, CO, USA. http://OpenMOPAC.net (accessed 29 June 2021).
27. J. J. P. Stewart, *Int. J. Quantum Chem.*, **58**, 133 (1996).
28. A. Li, H. S. Muddana and M. K. Gilson, *J. Chem. Theory Comput.*, **10**, 1563 (2014).
29. C. R. A. Daniel, N. M. Rodrigues, N. B. Costa Jr. and R. O. Freire, *J. Phys. Chem. C*, **119**, 23398 (2015).
30. M. Enescu, J. Ridard, V. Gheorghe and B. Levy, *J. Phys. Chem. B*, **106**, 176 (2002).
31. W. Xiaoyan, Y. Sun, D. Pan, Z. Niu, Z. Xu, Y. Jiang, W. Wu, Z. Li, L. Zhang and Q. Fan, *Appl. Clay Sci.*, **183**, 105363 (2019).
32. Y. Lu, W. Wang, Q. Wang, J. Xu and A. Wang, *Appl. Clay Sci.*, **183**, 105301 (2019).
33. D. Huang, Y. Zheng and Q. Quan, *Appl. Clay Sci.*, **183**, 105314 (2019).
34. F. R. G. V. Rosendo, L. I. F. Pinto, I. S. de Lima, P. Trigueiro, L. M. d. C. Honório, M. G. Fonseca, E. C. Silva-Filho, A. B. Ribeiro, M. B. Furtini and J. A. Osajima, *Appl. Clay Sci.*, **188**, 105499 (2020).
35. J. A. Cecilia, E. Vilarrasa-García, C. L. Cavalcante, D. C. S. Azevedo, F. Franco and E. Rodríguez-Castellón, *J. Environ. Chem. Eng.*, **6**, 4573 (2018).
36. D. Wang, L. Zhu, J. Qiu and P. Zhu, *Appl. Clay Sci.*, **185**, 105421 (2020).
37. N. Frini-Srasra and E. Srasra, *Desalination*, **250**, 26 (2010).
38. J. Zhu, P. Zhang, Y. Wang, K. Wen, X. Su, R. Zhu, H. He and Y. Xi, *Appl. Clay Sci.*, **159**, 60 (2018).
39. C. Wang, X. Zou, H. Liu, T. Chen, S. L. Suib, D. Chen, J. Xie, M. Li and F. Sun, *Appl. Surf. Sci.*, **486**, 420 (2019).
40. T. A. Saleh and V. K. Gupta, *Curr. Nanosc.*, **8**, 739 (2012).
41. Q. Chen, R. Zhu, L. Deng, L. Ma, Q. He, J. Du, H. Fu, J. Zhang and A. Wang, *Chem. Eng. J.*, **378**, 122131 (2019).
42. M Zhang, J. Lu, C. Zhu, Y. Xiang, L. Xu and T. Chen, *Solid State Sci.*, **90**, 76 (2019).
43. A. Amari, H. Gannouni, M. I. Khan, M. K. Almesfer, A. M. Elkhaleefa and A. Gannouni, *Appl. Sci.*, **8**, 2302 (2018).
44. S. Ardizzone, C. L. Bianchi, M. Fadoni and B. Vercelli, *Appl. Surf. Sci.*, **119**, 253 (1997).
45. S. Bentahar, A. Dbik, M. E. Khomri, N. E. Messaoudi and A. Lacherai, *J. Environ. Chem. Eng.*, **5**, 5921 (2017).
46. G. Wang. Y. Zhang, S. Wang, Y. Wang, H. Song, S. Lv and C. Li, *Environ. Sci.: Water Res. Technol.*, **6**, 1568 (2020).
47. M. Shaban, M. R. Abukhadra, A. A. P. Khan and B. M. Jibali, *J. Taiwan Inst. Chem. Eng.*, **82**, 102 (2018).
48. M. F. Oliveira, M. G. C. Silva and M. G. A. Vieira, *Appl. Clay Sci.*, **168**, 366 (2018).
49. I. Langmuir, *J. Am. Chem. Soc.*, **38**, 2221 (1918).
50. T. Li, T. Liao, X. Su, X. Yu, B. Han, Y. Zhu and Y. Zhang, *Environ. Sci.: Water Res. Technol.*, **4**, 1671 (2018).
51. K. G. Bhattacharyya and S. S. Gupta, *Desalination*, **272**, 6 (2011).
52. L. Mouni, L. Belkhiri, J.-C. Bollinger, A. Bouzaza, A. Assadi, A. Tirri, F. Dahmouni, K. Madani and H. Remini, *Appl. Clay Sci.*, **153**, 38 (2018).
53. W. Hajjaji, S. Andrejkovičová, D. M. Tobaldi, A. Lopez-Galindo, F. Jammoussi, F. Rocha and J. A. Labrincha, *Clay Minerals*, **51**, 19 (2016).
54. O. Amrhar, H. Nassali and M. S. Elyoubi, *J. Material Environ. Sci.*, **6**, 3054 (2006).
55. T. Ngulube J. R. Gumbo, V. Masind and A. Maity, *J. Mol. Struct.*, **1184**, 389 (2019).
56. J. Liu, N. Wang, H. Zhang and J. Baevens, *J. Environ. Conv. Manag.*, **238**, 473 (2019).
57. C. Tian C. Feng, M. Wei and Y. Wu, *Chemosphere*, **208**, 476 (2018).
58. A. Ausavasuki, C. Kampoosaen and O. Kengnok, *J. Clen. Prod.*, **134**, 506 (2016).
59. M. Chahkandi, *Material Chem. Phys.*, **202**, 340 (2017).
60. G. Crini and P.-M. Badot, *Prog. Polym. Sci.*, **33**, 399 (2008).
61. T. Panczyk, P. Wolski, A. Jagusiak and M. Drach, *RSC Adv.*, **4**, 47304 (2014).
62. L. Zhou, R. Johnson, T. Habteyes and H. Guo, *J. Chem. Phys.*, **146**, 164701 (2017).
63. R. G. Huber, M. A. Margreiter, J. E. Fuchs, S. von Grafenstein, C. S. Tautermann, K. R. Liedl and T. Fox, *J. Chem. Inf. Model.*, **54**, 1371 (2014).

Supporting Information

Eco-friendly adsorption of dye pollutants by palygorskite in aqueous effluents: Experimental and computational studies

Anne Beatriz Figueira Câmara[*,†], Rafael Viana Sales[*], Carlos Vital dos Santos Júnior[****], Miguel Angelo Fonseca de Souza[****], Clenildo de Longe[*], Thiago Medeiros Chianca[*], Rosangela Dala Possa[**], Luiz Carlos Bertolino[***], and Luciene Santos de Carvalho[*,†]

*Institute of Chemistry, Federal University of Rio Grande do Norte, Energetic Technologies Research Group, 59078-900, Natal, Brazil

**Mineral Technology Center, 21941-908, University City, Rio de Janeiro, Brazil

***Xingu Study Institute, Federal University of the South and Southeast of Pará, 68380-000, São Félix do Xingu-PA, Brazil

****Laboratory of Computational Chemistry, Institute of Chemistry, Federal University of Rio Grande do Norte, 59078-900, Natal, Brazil

(*Received 9 September 2021 • Revised 21 February 2022 • Accepted 4 March 2022*)

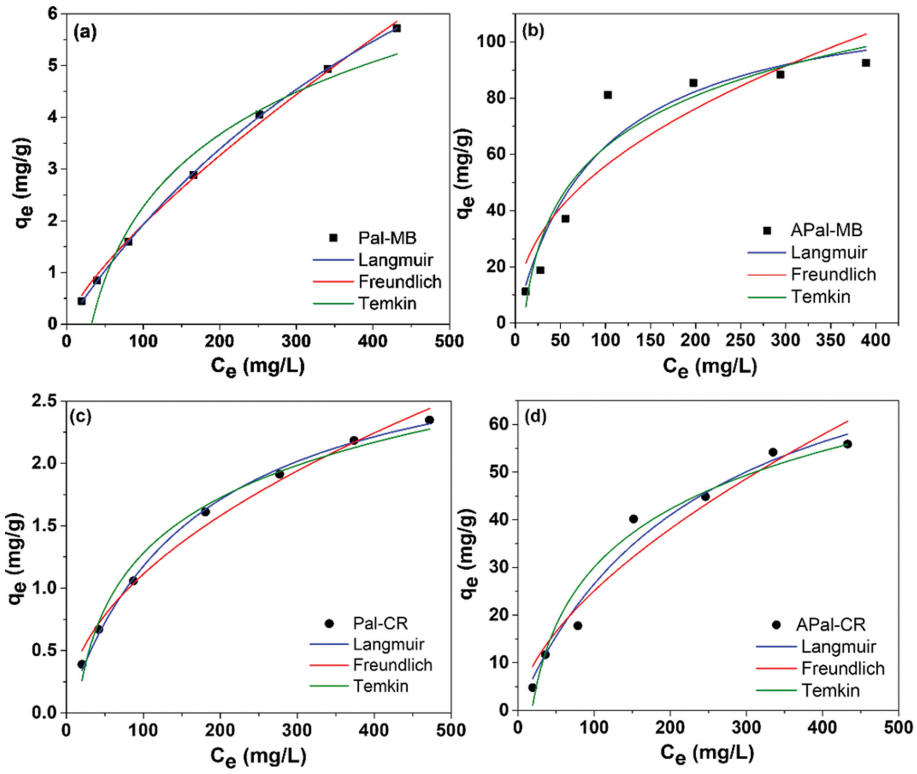

Fig. S1. Non-linear adjustment of Langmuir, Freundlich and Temkin adsorption isotherms for (a) Pal-MB, (b) APal-MB, (c) Pal-CR e (d) APal-CR interactions.

Table S1. Absorption features of Pal and APal

Wavenumber (cm^{-1})	Absorption feature
3,695	Al-OH stretching vibration
3,613	Stretch vibrations of the structural hydroxyl groups, (Fe-OH, Mg-OH) and (Al-OH, Mg-OH)
3,535	Stretch vibration -Si-OH
2,920 to 3,786 and 1,648	Stretching vibration of hydroxyl groups (-OH)
910	Al-OH-Al flexion
981	Asymmetric elongation Si-O-Mg
795	Stretching vibration of Si-O-Si

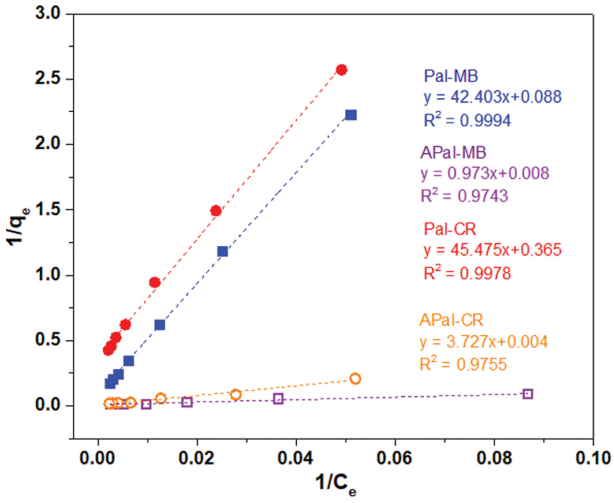

Fig. S2. Linear adjustment of Langmuir adsorption isotherm for the studied adsorbents.

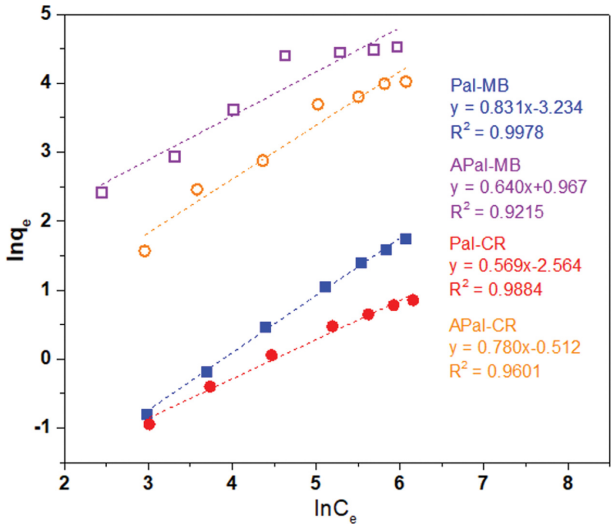

Fig. S3. Linear adjustment of Freundlich adsorption isotherm for the studied adsorbents.